J. Mech. Phys. Solids 195 (2025) 105931

Contents lists available at ScienceDirect

Journal of the Mechanics and Physics of Solids

journal homepage: www.elsevier.com/locate/jmps

Fracture of polymer-like networks with hybrid bond strengths

Chase M. Hartquist [a], Shu Wang [a,b], Bolei Deng [c], Haley K. Beech [b,d], Stephen L. Craig [b,e], Bradley D. Olsen [b,d], Michael Rubinstein [b,e,f,g], Xuanhe Zhao [a,h,*]

[a] Department of Mechanical Engineering, Massachusetts Institute of Technology, Cambridge, MA 02139, USA
[b] NSF Center for the Chemistry of Molecularly Optimized Networks, Duke University, Durham, NC 22708, USA
[c] Daniel Guggenheim School of Aerospace Engineering, Georgia Institute of Technology, Atlanta, GA 30332, USA
[d] Department of Chemical Engineering, Massachusetts Institute of Technology, Cambridge, MA 02139, USA
[e] Department of Chemistry, Duke University, Durham, NC 22708, USA
[f] Departments of Mechanical Engineering and Materials Science, Biomedical Engineering, and Physics, Duke University, Durham, NC 22708, USA
[g] Institute for Chemical Reaction Design and Discovery, Hokkaido University, Sapporo, 001-0021, Japan
[h] Department of Civil and Environmental Engineering, Massachusetts Institute of Technology, Cambridge, MA 02139, USA

ARTICLE INFO

MSC:
74A45

Keywords:
Fracture
Fatigue
Polymer
Metamaterials
Percolation

ABSTRACT

The design and functionality of polymeric materials hinge on failure resistance. While molecular-level details drive crack evolution in polymer networks, the connection between individual chain scission and bulk failure remains unclear and difficult to probe. In this work, we systematically study the fracture mechanics of polymer-like networks with hybrid bond strengths. We reveal that varying the ratio of strong and weak strands within otherwise identical networks gives a non-monotonic relationship between intrinsic fracture energy and strong strand fraction. Networks with some weak strands can counterintuitively outperform those with exclusively strong strands. Experiments on poly(ethylene glycol) gels and architected polymer-like lattices together with simulations unveil these properties. We show through computational visualization that strand type concentrations impact crack growth patterns and fracture energy trends. Cracks propagate through weak layers at low strong strand fractions. Aggregate clusters deflect or pin cracks at similar concentrations of strong and weak strands. Cracks blunt due to dispersed weak strand failure at high strong strand fractions. The sacrificial weak strands can notably deconcentrate stress near the crack tip, which toughens by delaying crack advancement. The interplay between concentration and clustering of strand types in networks with hybrid bond strengths, combined with crack growth phenomena and nonlocal energy release, provides insights into unusual fracture characteristics. Results shed light on fracture in polymer networks and percolated lattices.

1. Introduction

From consumer goods like automobile tires, contact lenses, and shoe soles to advanced applications in engineered tissues, fluidic actuators, and drug delivery vehicles, polymer networks exist universally throughout society. These products require polymeric materials with sufficient integrity to sustain repeated use (Creton and Ciccotti, 2016; Zhao et al., 2021). Although imperative for material design, selection, durability, and safety, the specifics of polymer fracture remain unclear. The key bottleneck lies in the challenge of connecting molecular structure, chain scission, network connectivity, and strand mechanics to the bulk-scale material separation that occurs during failure.

* Corresponding author at: Department of Mechanical Engineering, Massachusetts Institute of Technology, Cambridge, MA 02139, USA.
E-mail address: zhaox@mit.edu (X. Zhao).

https://doi.org/10.1016/j.jmps.2024.105931
Received 24 July 2024; Received in revised form 30 October 2024; Accepted 31 October 2024
Available online 10 November 2024

In fracture mechanics, intrinsic fracture energy — the minimum energy required to propagate a crack per newly created surface area — characterizes the resistance of materials to crack extension during loading (Rivlin and Thomas, 1953). This value can match the fatigue threshold — the critical energy release rate under which a fatigue crack will not grow during cyclic loading — in elastic networks under the single-process hypothesis of slow crack extension (Tang et al., 2017). Griffith first proposed a theory linking atomic-scale bond patterns with bulk-scale fracture behavior of brittle materials. He predicted a direct relationship between intrinsic fracture energy Γ_0 and the energy required to break bonds along the crack plane as

$$\Gamma_0/M = U_{\text{bond}}, \tag{1}$$

where M is the areal density of bonds intersecting the crack plane in the reference state and U_{bond} is the total bond dissociation energy to break an atomic bond (Griffith, 1921). Experiments on crystalline materials support this theory for brittle fracture. Lake and Thomas built on this framework to explore the molecular picture of fracture in polymer networks. Unlike brittle materials with packed atomic bonds, polymer networks contain interconnected strands of bonded monomers. Their model predicts that the intrinsic fracture energy of a polymer network is the energy required to break strands along the crack plane as

$$\Gamma_0/M = U_{\text{strand}}, \tag{2}$$

where M is the areal density of strands intersecting the crack plane in the reference state and U_{strand} is the energy to break each polymer strand (Lake and Thomas, 1967). The intrinsic fracture energy predicted here excludes contributions of bulk dissipation to crack propagation (Zhao, 2014; Bai et al., 2019). Lake and Thomas also proposed that the energy to break a strand relates to the bond dissociation energy U_{bond} as

$$U_{\text{strand}} = NU_{\text{bond}}, \tag{3}$$

where N is the number of repeating monomers in a given strand. This physically suggests that all bonds along the bridging strand are stretched near rupture at the strand scission event. This approximation has been broadly adopted and can provide reasonable estimates for the intrinsic fracture energy of polymer networks. However, recent single molecule force spectroscopy measurements and atomic simulations find that U_{strand} is about 6–10 times smaller than NU_{bond} (Wang et al., 2019; Smith et al., 1996). As a result, Lake-Thomas model predictions underestimate the magnitudes of the intrinsic fracture energies from recent experiments by ~1–2 orders (Lin and Zhao, 2020; Akagi et al., 2013; Barney et al., 2022; Wang et al., 2021).

Polymer-like network models provide an alternative approach to investigating the quantitative and qualitative contributions of strands to fracture across length scales. Fracture studies on polymer-like networks can directly describe the mechanics of soft architected materials and indirectly provide insights into mechanisms surrounding failure in some polymer systems. Inspired by macroscopic soft metamaterials (Yamaguchi et al., 2020) and coarse-grained or mesoscale simulations (Lei et al., 2021; Ghareeb and Elbanna, 2020; Lei and Liu, 2022; Picu and Jin, 2023), polymer-like networks apply the constitutive behaviors experimentally measured for polymers to describe strand deformation within connected lattices (Deng et al., 2023; Hartquist et al., 2024). In simulations, this approach gives improved computational efficiency compared with molecular dynamics, permitting realistic domain sizes for fracture studies. This method tracks details for each strand during bulk deformation and fracture processes. In experiments, architected materials with strain-hardening strand behavior can be fabricated to provide insights into how the mechanics of constituents relate to bulk performance. Real polymer networks differ from polymer-like analogs due to detailed contributions from molecular interactions, polydispersity, defects, solvent, etc. Polymer-like network fracture studies have explained nonlocal intrinsic fracture energy (Deng et al., 2023) and predicted the intrinsic fracture energy measurements from recent polymer experiments (Hartquist et al., 2024). While traditional lattice models have been employed to study the effects of irregular or hybrid networks on mechanics (Malakhovsky and Michels, 2007; Deogekar and Picu, 2018; Borodulina et al., 2018), these models have yet to fully explain the complex fracture behavior that arises in polymer-like networks.

Here, we explore the fracture mechanics of polymer-like networks with hybrid bond strengths. We systematically tune the ratios of weak and strong strands within networks through simulations and experiments. We then conduct the pure shear fracture test to measure the fracture energies of these networks across different concentrations. The simulation results give rise to a non-monotonic relationship between intrinsic fracture energy and strong strand fraction. Notably, the fracture energy of a network with some weak strands can overshoot that of a network with only strong strands. We visualize, analyze, and compare the fracture mechanisms governing crack growth in simulations. With varying fractions of strong and weak strands, we show that crack growth patterns change. First, at low strong strand fractions, cracks traverse directly through layers of weak strands. Second, with increasing strong strand concentration, cracks deflect in the presence of clusters or fully connected structures of strong strands. Third, past the percolation threshold, crack pinning occurs in the presence of percolated strong networks. Fourth, with few remaining weak strands, cracks blunt as dilute weak strands break, deconcentrating stress from the crack tip. A systematic understanding of the fracture mechanics of polymer-like networks with hybrid bond strengths can shed light on the fracture of real polymer networks. Note that we do not simulate real polymers; the conclusions remain within the domain of polymer-like networks.

The outline of this paper is as follows. In Section 2, we introduce the experimental methods for fabricating, testing, and evaluating polymer and polymer-like networks with hybrid bond strengths. Section 3 describes the mathematical model and computational approach to simulating polymer-like network fracture. Section 4 highlights the experimental trends in fracture energy for hybrid poly(ethylene glycol) (PEG) networks crosslinked by various concentrations of mechanophores displaying two distinct breaking forces. It also provides a similar analysis for hybrid polymer-like network simulations supplied with PEG-like strands governed by parameters in the modified freely jointed chain model supplied by experiments. In Section 5, we report the qualitative fracture phenomena observed during these simulations, fracture energy enhancement achieved by adding small fractions of weak strands, and nonlocal energy release detected when the bridging strand breaks. We conclude in Section 6 with remarks on the broader implications of these findings.

2. Experiments

2.1. Polymer network fabrication

Tetra-PEG gels are made to largely duplicate the systems reported previously by Beech et al. (2023). The weak linker (WL) and strong linker (SL) are the same as those used by Beech et al. (2023). For each gel, 505.4 mg (25 mM) of azide-functionalized PEG is dissolved in 2 mL of anhydrous propylene carbonate in a glovebox. The weak linkers (WL) and strong linkers (SL) are weighed into a vial and dissolved in 1.59 mL propylene carbonate for transfer to the pre-polymer solution. The resulting solution is vortexed before adding 0.405 mL of the 84.9 mg/mL copper catalyst solution. The solution is then transferred to a $5.5 \times 10 \times 0.1$ cm Teflon mold with an 18-gauge syringe, gently tapped to eliminate bubbles, and left to react in the glovebox for 24 h.

2.2. Polymer network mechanical testing

Rheological measurements are conducted on an Anton Paar MCR 301 rheometer with a disposable 10 mm parallel plate geometry. Samples are cut to size with a 10 mm diameter biopsy punch. The plates are covered with adhesive sandpaper to prevent slipping (Norton, A275, 120 grit, Aluminum Oxide). Frequency sweep measurements are conducted at 23 °C with a constant 0.5% shear strain, well within the linear viscoelastic regime based on initial strain sweeps. A Peltier temperature control stage maintains a constant sample temperature. Three samples from different locations throughout the gel are punched out for each measurement of shear modulus.

Samples for fracture energy measurement are cut with a razor blade into a 20×20 mm square. This is reduced to a 20×4 mm exposed surface after clamping. Each measurement employs 3 unnotched samples and 5 notched samples. A 5 mm edge cut is made in the center of one side of each notched specimen perpendicular to the sample loading direction. The exact thickness, width, and cut length are measured with calipers and a ruler before deformation. Samples are loaded into the clamps at a gauge length of about 2 mm then stretched to a force of 0.01 N, which results in an initial gauge length of 4 ± 0.5 mm. Samples are loaded to failure at a constant strain of 0.011 mm/s (0.66 mm/min) to avoid bulk hysteresis and dissipation. Fracture energy is calculated using the Thomas-Rivlin method (Rivlin and Thomas, 1953) where the strain energy is obtained by integrating the unnotched stress-stretch curve to the critical stretch at which the crack of the notched sample begins to propagate.

2.3. Architected network fabrication

Specimens are fabricated by laser cutting Wear-Resistant Easy-to-Machine Acetal Films (12" × 12" × 0.003") (McMaster-Carr part number: 5742T11) using an EpilogLaser Fusion Maker 40 W laser machine. Each strand exhibits a "zigzag" structure that initially unfolds to provide an soft bending modulus, followed by material deformation to provide a stiff stretching modulus (Fig. 11a) (Jang et al., 2015). This large discrepancy between stiffness mimics the J-shaped force-extension behavior of polymer chains. The pattern is designed in CorelDraw to contain 30 layers of square repeating units with 62 strands per layer (Fig. 11b). The undeformed height of the whole network is 120 mm, and the distance between two neighboring junctions is $4\sqrt{2}$ mm. The distance between the laser head and the acetal film is calibrated as instructed in the operation manual of the laser cutter to ensure sharp focus. The parameters are chosen to be 15% of the maximum laser power, 25% of the frequency, and 90% of the speed. An unnotched sample with identical strands, two notched samples with identical strands, and three notched samples with different precut strands are fabricated (Fig. 11). The locations of the precut strands are determined based on the measurements of the networks without selective precut strands and numerical simulations. Details of the notched sample preparation with selected precut strands are explained in the next section. For each sample, four 1/16" acrylic sheets are cut and glued onto the front and the back of the uncut portion to act as rigid boundary (Fig. 11b), which is clamped onto the mechanical testing machine.

2.4. Architected network mechanical testing

Mechanical tests are performed on a ZwickiLine tensile testing machine (Zwick Roell). We conduct uniaxial extension on an unnotched sample at a loading rate of 200 mm/min to measure the critical energy release rate of networks comprised of identical strands, as depicted by the solid black line in Fig. 11c of the manuscript. The force-stretch curve of an unnotched sample is measured first. We then identify the effective force-stretch curve for each strand within the network (the curve shown in Fig. 11a of the manuscript) based on measurements of individual lasercut strands and simulations such that simulated unnotched uniaxial extension profiles match the experimental measurements. For the notched networks with identical strands, we introduce a notch at the same position on each sample. Uniaxial tensile tests are performed at a loading rate of 200 mm/min. Since strand rupture is uncontrolled when a notched sample is loaded to the fracture event, we preset the critical stretch for the whole network instead of actually fracturing the network, and we consider the bridging strand to have "ruptured" when the whole network reaches this critical stretch. This strategy dictates the failure force and stretch of the strands. The critical stretch is set to be 4.47 for a network with 100% strong strands ($\phi_S = 100\%$), and the single-strand critical displacement of the bridging chain is measured to be 20.3 mm. Note that the critical stretch of the whole network is chosen arbitrarily. A stretch of 4.47 is chosen because the sample is visually highly stretched, but the bridging strand has not yet broken. Therefore, the displacement of the bridging strand can be measured with calipers. The energy release rate at the stretch of 4.47 is considered to be the intrinsic fracture energy Γ_0 of the network. By integrating the force-stretch curve of the unnotched sample to the stretch of 4.47 and multiplying by the initial height of the network

$h_0 = 120.0$ mm, we obtain the intrinsic fracture energy to be $\Gamma_0 = 0.659$ J. We approximate this test to pure shear with a relaxed incompressibility assumption. For the 0% strong strand network ($\phi_S = 0\%$), the critical stretch of the whole network is preset to be 4.07, and the critical displacement of the weak bridging strand was measured to be 18.78 mm. The fracture energy is $\Gamma_0 = 0.327$ J. With the experimental data for $\phi_S = 100\%$ and $\phi_S = 0\%$, we then algorithmically select random distibutions of strong and weak strands within networks with $\phi_S = 30\%$, 80%, and 95% and simulate the full loading behavior of unnotched and notched specimens using the approximate pure shear test. We record intrinsic fracture energy of $n \geq 5$ samples for a given ϕ_S and store the locations of each strand that breaks in a notched sample prior to reaching the critical height h_c along with the bridging strand that breaks at h_c. Note that the bridging strand in heterogeneous hybrid networks is not necessarily the strand at the tip of the crack; simulations inform detection of this strand in experiments. We select representative patterns from simulations for experiments, supply them to fabricated notched architected networks, and precut the strands that break prior to h_c, for h_c is the only outcome of interest from the notched extension experiment. The three notched samples with intentionally precut strands, representing selected cases at $\phi_S = 30\%$, 80%, and 95%, are extended to the point where the bridging strands reach their critical displacements. At these critical points, the overall stretch of the entire notched network experimentally reaches 4.208, 4.458, and 4.580 for $\phi_S = 30\%$, $\phi_S = 80\%$, and $\phi_S = 95\%$, respectively. By integrating the stress-stretch curve of the unnotched sample to the critical stretches and multiplying the initial height of the network (120 mm), we obtain the fracture energies to be $\Gamma = 0.402$, 0.645, and 0.844 J. It is noteworthy that the fracture energy of $\phi_S = 95\%$ network is 1.28 times that of the $\phi_S = 100\%$ network.

3. Simulations

3.1. Mechanical response of strands

We model strands within polymer-like networks by applying the mechanical response of typical strands to edges in a lattice. Experiments characterize the force-extension dependence of polymers with various chemistries through single molecule force spectroscopy (SMFS). We adopt the modified freely jointed chain model (m-FJC) to parametrize these responses (Smith et al., 1996), which relates the force f to the end-to-end distance r as

$$\frac{r}{l_0} = \left[\coth\left(\frac{f}{K_S}\right) - \frac{K_S}{f}\right]\left(1 + \frac{f}{K_E}\right) \tag{4}$$

for networks of polymer chains with contour lengths l_0. The Langevin function within this model captures the conformational entropy change from uncoiling polymer chains through a modulus K_S and the energy change from stretching and bending backbone bonds through a modulus K_E. Polymer chains typically exhibit a stark contrast between K_E and K_S, which gives $K_E/K_S \sim 10^4$ (Zhang and Zhang, 2003). We convert this relation to describe the force-stretch behavior by relating the contour length and end-to-end distances as

$$r = \lambda r_0, \text{ and } l_0 = \lambda_{lim} r_0, \tag{5}$$

where r_0 is the undeformed end-to-end distance and λ_{lim} is the transition stretch between the entropic and energetic regimes. The m-FJC model (4) can be reformulated to relate force f and stretch λ as

$$\frac{\lambda}{\lambda_{lim}} = \left[\coth\left(\frac{f}{K_S}\right) - \frac{K_S}{f}\right]\left(1 + \frac{f}{K_E}\right). \tag{6}$$

The m-FJC model provides the constitutive framework assigned to nonlinear springs to describe each strand within the network simulation. We select PEG as the representative polymer for both simulations and experiments. Previous studies suggest that $K_S = 5.86$ pN and $K_E = 105$ nN for PEG, which gives a ratio of $K_E/K_S \approx 1.8 \times 10^4$ (Oesterhelt et al., 1999). We also prescribe the transition stretch λ_{lim} and f_f from experiments. We choose λ_{lim} based on the typical contour length of strands and f_f based on the strength of the mechanophore linkers with different reactivities (Beech et al., 2023). These selections constrain the breaking stretch λ_f via the m-FJC model (6). We choose $\lambda_{lim} = 5$ for simulations. This models the λ_{lim} of a linear PEG chain with a molecular weight of around 3.4 kDa. We also select $f_f = 1$ nN and 5 nN for weak and strong strands in simulations, respectively (Fig. 1a), which are comparable in magnitude to $f_f \sim 0.7$ nN and 3–4 nN found for strands in experimental PEG networks (Bowser et al., 2021; Wang et al., 2021). While the breaking force and stretch can deviate in PEG experiments, all strands in simulations of a given type exhibit the mechanical behavior from Fig. 1a. Experiments with PEG gels (Fig. 1b) and simulations with PEG-like strands (Fig. 1c) are then fabricated or assembled for fracture testing.

3.2. Mathematical model for simulations

To simulate entire networks, we enforce the force-stretch behavior from the m-FJC model for PEG across a collection of e edges connecting n nodes, which respectively mimic strands and crosslinks within polymer networks. We predefine nodes as the coordinates of square two-dimensional lattice topologies for all samples. Coordinates take the form (x_i, y_i) for $i = 1, \ldots, n$ in Cartesian space, where i is the node number. Note that here we present the general 3D formulation where the z-direction describes the sample thickness but neglect these terms in the 2D special case employed throughout this study. We treat edges as nonlinear springs with initial end-to-end lengths controlled by node coordinates and deformation responses described by the m-FJC model (6) (Mao et al., 2017; Talamini et al., 2018). Two matrices store nodes and edges for simulations in MATLAB. The first stores node positions via coordinates in columns and numbers these nodes by row. The second stores the nodes each edge connects via two node numbers

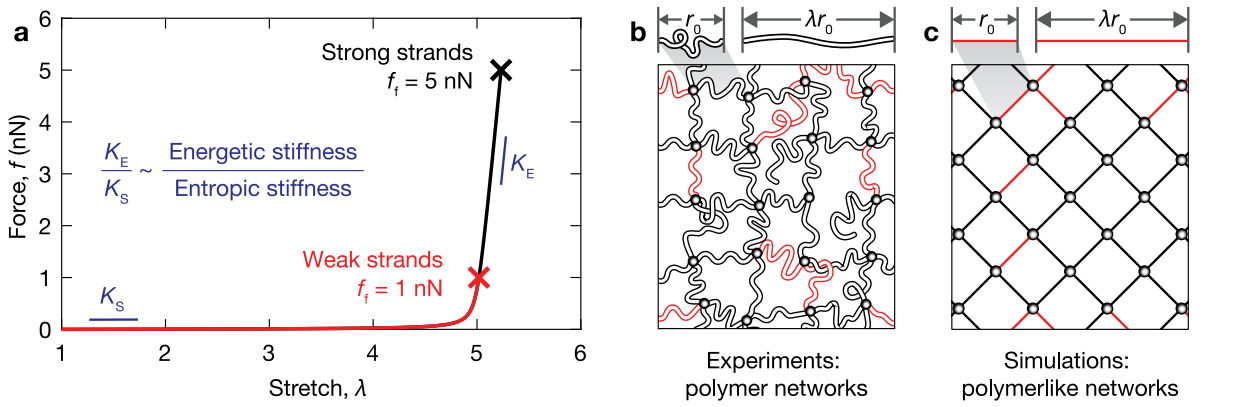

Fig. 1. (a) Hybrid networks contain randomly assigned weight fractions of strong strands (black) and weak strands (red), which rupture at breaking forces of $f_f = 1$ and 5 nN in simulations, respectively. The m-FJC model defines the ratio of energetic (K_E) to entropic (K_S) stiffness of polymer-like strands (depicted) to match experimentally the highly nonlinear mechanical behavior measured for PEG ($K_E/K_S = 1.8 \times 10^4$). (b) Experiments of PEG gels and (c) simulations of polymer-like networks stretch strands from their undeformed length (r_0) to arbitrary lengths (λr_0) during sample loading.

in columns and numbers these edges by row. We apply boundary conditions to various nodes, solve the boundary value problem, and iterate to perform quasi-static mechanical tests. The pure shear fracture test is conducted to quasi-statically stretch notched and unnotched specimens from an initial height h_0 through various heights h in the y-direction by implementing the following clamped boundary conditions on the nodes at the top and bottom of the sample as

$$\begin{aligned} y_i &= h, \text{ for } i \in \text{top nodes}, \\ y_i &= y_i^0, \text{ for } i \in \text{bottom nodes}, \end{aligned} \tag{7}$$

where y^0 is the initial y-coordinate of the node. The pure shear loading condition is typically enforced experimentally in 2D by selecting a geometry where the width far exceeds the height of the sample. Pure shear can be enforced strictly by applying boundary conditions to fix the x-displacement on the right and left nodes on the sample as

$$\begin{aligned} x_i &= x_i^0, \text{ for } i \in \text{left nodes}, \\ x_i &= x_i^0, \text{ for } i \in \text{right nodes}, \end{aligned} \tag{8}$$

where x^0 is the initial x-coordinate of the node. We impose equilibrium onto all remaining nodes by first calculating the stored system energy within the sample. The stretch λ_{ij} of the edge connecting nodes i and j is first defined as

$$\lambda_{ij} = r_0^{-1} \sqrt{(x_i - x_j)^2 + (y_i - y_j)^2 + (z_i - z_j)^2}, \tag{9}$$

where r_0 is the distance between nodes in the undeformed configuration. The stored energy is then calculated as

$$U_{\text{total}} = \sum_{i,j} \int_1^{\lambda_{ij}} f(\lambda'_{ij}) d\lambda'_{ij}, \tag{10}$$

where $f(\lambda'_{ij})$ is the force-stretch response of the selected edge. Note that for hybrid networks, the function $f(\lambda'_{ij})$ differs between weak and strong strands. We then employ Newton's method to minimize the system energy such that

$$\frac{\partial U_{\text{total}}}{\partial x_i} = 0, \quad \frac{\partial U_{\text{total}}}{\partial y_i} = 0, \text{ and } \quad \frac{\partial U_{\text{total}}}{\partial z_i} = 0 \tag{11}$$

across the lattice. Energy minimization is repeated for quasi-static loading at discretized displacements prescribed on the top surface each until a termination criterion is met. Strand fracture occurs when the equilibrated stretch of an edge exceeds the fracture stretch of the strand, i.e., $\lambda_{ij} > \lambda_f$. Fractured strands are removed by deleting the relevant entries of the edge storage matrix. Energy minimization is repeated at that step before further displacing the sample.

3.3. Numerical solver implementation

The numerical solver captures this system state, minimizes the energy, and solves for each discrete response using Newton's method. Lattice coordinates can be succinctly written in vector form as

$$\mathbf{X} = [x_1, y_1, z_1, x_2, y_2, z_2, \ldots, x_n, y_n, z_n]^{\mathrm{T}}, \tag{12}$$

where the vector $\mathbf{X}$ is the node matrix with size $2n \times 1$ in 2D ($3n \times 1$ in 3D). The generalized set of problems solvable by Newton's method, postulated first in (11), can be written in vector form as

$$\mathbf{F}(\mathbf{X}) = \mathbf{0}, \tag{13}$$

where $\mathbf{F}(\mathbf{X})$ is the functional form of the nonlinear system. Here, this describes the system energy minimization from (10) and (11). This problem formulates the system of nonlinear equations necessary to solve for $\mathbf{X}$. The generalized Newton's method is undertaken to numerically solve for the root of $\mathbf{F}$ in a Banach space as

$$\mathbf{X}_{l+1} = \mathbf{X}_l - \left[\mathbf{J}(\mathbf{X}_l)\right]^{-1} \mathbf{F}(\mathbf{X}_l), \tag{14}$$

where $\mathbf{J}$ is the Jacobian and l describes the internal iteration number within the method. We update the stored Jacobian from the prior iteration instead of recalculating it stepwise to improve efficiency as follows:

$$\mathbf{J}(\mathbf{X}_l)\left(\mathbf{X}_{l+1} - \mathbf{X}_l\right) = -\mathbf{F}(\mathbf{X}_l). \tag{15}$$

This formulation provides sequential approximations $\mathbf{X}_l$ from an initial guess $\mathbf{X}_0$. The method concludes once an accuracy requirement δ is met, which is defined as

$$\|\mathbf{X}_{l+1} - \mathbf{X}_l\| < \delta. \tag{16}$$

The discretized quasi-static loading scheme provided by the boundary conditions completes P steps from $p = 1, \ldots, P$ to stretch the network until the simulation terminates. Newton's method (13) occurs at each step p to provide the updated system state $\mathbf{X}^p$. The current $\mathbf{X}^p$ is selected as the input guess for the next step to accelerate Newton's method in converging towards $\mathbf{X}^{p+1}$.

3.4. Polymer-like network simulations

We measure fracture energy (Fig. 2a) and intrinsic fracture energy (Fig. 2b) through simulations on networks comprised of weak and strong strands whose force-stretch behaviors match that of Fig. 1a. We systematically vary the concentration of strong strands within the network from 0% to 100%. Strand type is allocated randomly in both notched and unnotched samples. Square lattices in 2D are constructed and set such that the undeformed sample width w_0 is twice the height h_0. First, we measure the critical height h_c by applying boundary conditions (7) and (8) to a sample with an edge crack perpendicular to the loading direction of length $w_0/2$ and quasi-statically loading the sample until the crack propagates (see Fig. 2c). We track the force on the top boundary (via the stored system energy) during the loading process as a function of the supplied displacement. The simulation program terminates once two failure criteria are met: at least one strand breaks, and the force drops below a threshold. Practically, we set the termination threshold force to 80% of the prior peak to maintain computational efficiency yet ensure the crack propagates sufficiently far. The critical height for crack propagation is then defined and measured as the height of the sample at the displacement corresponding to the maximum force readout of the entire loading procedure. We measure the critical height for at least four samples, each containing a distinct random assignment of strand types.

Second, we record the stress-height response of unnotched samples during quasi-static loading in pure shear up to h_c by tracking force and displacement (Fig. 2d). To measure fracture energy, we extract the loading curve to each of the four critical heights for four unnotched samples with random strand assignments. We calculate fracture energy from this response by integrating the nominal stress S up to h_c as

$$\Gamma = \int_{h_0}^{h_c} S\, dh. \tag{17}$$

To measure intrinsic fracture energy, we perform a quasi-static cyclic loading and unloading procedure between h_0 and h_c. Strands that break during loading remain broken during unloading. This can be repeated to determine the stress-height response across arbitrary cycle numbers n. Since we treat strands as ideally elastic, all dissipation occurs during the first loading cycle such that the unloading stress-height response will match that of any future loading cycles to h_c. Therefore, we only perform one loading and unloading cycle to determine the intrinsic response. We calculate intrinsic fracture energy by integrating the unloading cycle from h_c to h_0 as

$$\Gamma_0 = -\int_{h_c}^{h_0} S\, dh. \tag{18}$$

3.5. Released and stored energy characterization

We collect the stored and released energy stepwise during the loading process in network simulations to study the energetic contributions of each strand to the fracture processes. The system energy calculation (10) sums the stored energy in each strand. We can separately save the stored energy for individual strands at a given loading step (U^p) as

$$U^p = \int_1^{\lambda^p} f(\lambda')d\lambda'. \tag{19}$$

The change in energy (ΔU) between two loading steps (e.g., p and $p+1$) can be measured as

$$\Delta U = \int_{\lambda^p}^{\lambda^{p+1}} f(\lambda')d\lambda'. \tag{20}$$

We measure and report the released energy of strands before and after a bridging strand breaks. We define released energy as ΔU such that p and $p+1$ are the equilibrated system states before and after breaking the strand, respectively. Note in this work we

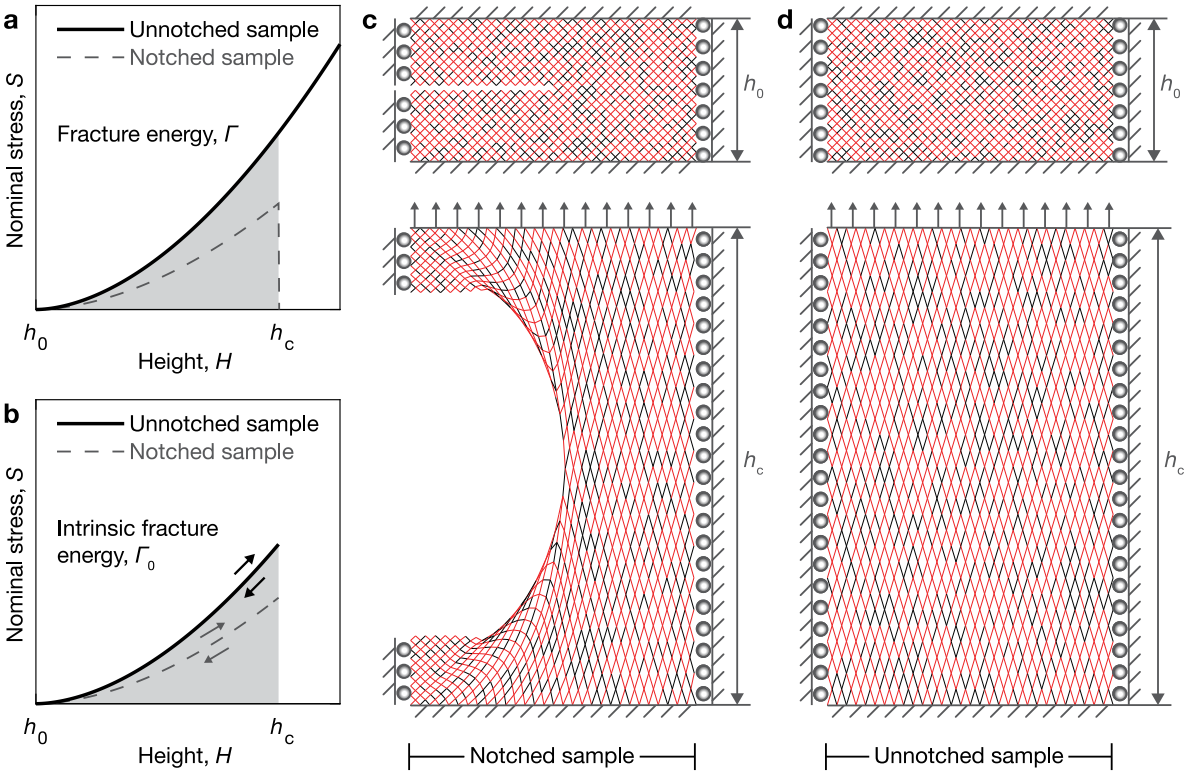

Fig. 2. A pure shear test is conducted to determine the (a) fracture energy Γ and (b) intrinsic fracture energy Γ_0 of polymer-like networks by uniaxially loading (c) the notched sample until the crack propagates at the critical height h_c. (d) The pristine monotonic and cyclic loading profiles of an unnotched sample to h_c are used to determine Γ and Γ_0. Black and red edges correspond to strands with strong and weak bond strengths.

report decreased stored energy as positive released energy. We apply these metrics in creating colormaps visualizing the energy distributions around a crack during fracture processes for hybrid polymer-like networks. As a control, we visualize the released energy from a network of strands with f_f and λ_f equivalent to that of strong strands but with linear elasticity. Simulation parameters for the network of linear strands are the same as those for all other hybrid networks.

3.6. Percolation theory

Connectivity and percolation of strands within networks before and after crack propagation impact fracture. The percolation threshold in polymers marks the critical concentration where a cluster of bonded strands spans the sample (Stauffer and Aharony, 2018; Rubinstein et al., 2003). This was first modeled for real polymer networks by Flory and Stockmeyer (Flory, 1942; Stockmayer, 1943).

Mathematical models and computations estimate the bond percolation thresholds for most common 2D and 3D lattices. In the fracture or fragmentation of networks, depercolation — marked by the same percolation threshold — describes the reverse process of severing a spanned network into clusters. Percolated and depercolated structures can influence the mechanical behavior of crack advancement during a fracture event. To account for this, Arora et al. incorporated depercolation of subnetworks by chain scission in developing a Micronetwork Fracture Theory (MFT) based on the Lake-Thomas model (Arora et al., 2020). Since the damage zone is larger than a single layer, this approach predicts a higher intrinsic fracture energy. Percolation theory can describe clustering and spanning behaviors of either weak or strong strands within a hybrid network. While most works studying percolation describe contexts where connections are either present or absent, this work introduces contexts where connections are either strong or weak strands. In hybrid networks, clustering and percolation analysis can describe both strand types within the same sample.

4. Results

4.1. Experiments

We crosslink tetra-PEG networks using two distinct mechanophores with different reactivities (Fig. 3a), producing networks with hybrid fractions of weak and strong strands. We supply the mechanophore crosslinkers with varying concentrations to directly influence the quantity of each strand type. We plot the fracture energy, normalized by that of a network formed with only strong

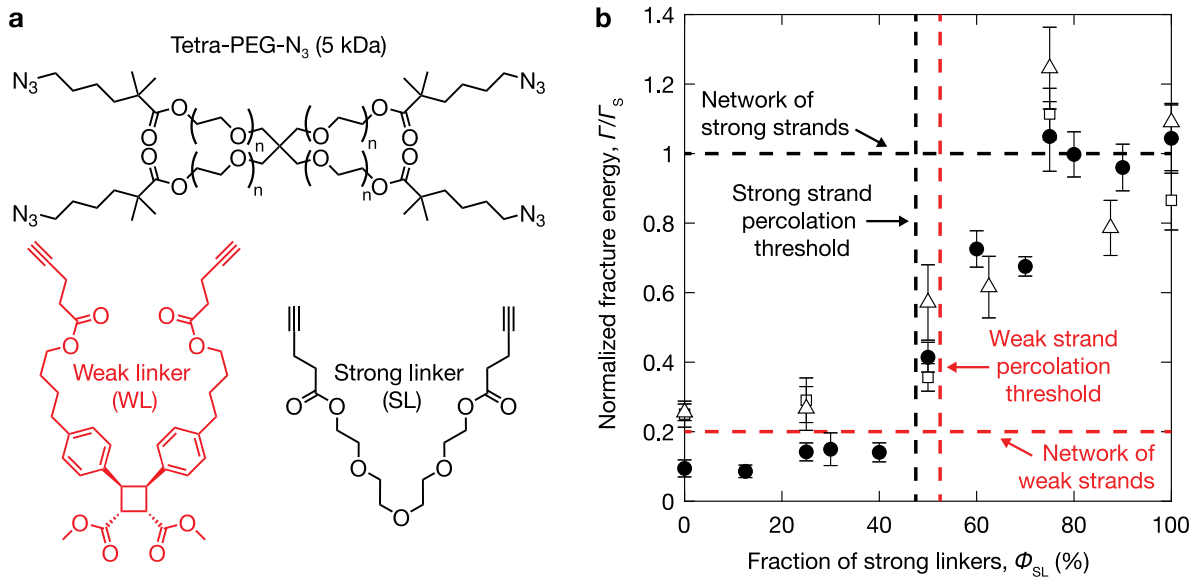

Fig. 3. (a) Chemistry of tetra-PEG gels with weak mechanophore (red, WL) and strong covalent (black, SL) linkers. (b) Fracture energy Γ of experimental networks with hybrid bond strengths normalized by that of a network of only strong strands Γ_S as a function of the strong strand fraction ϕ_S. Vertical lines mark experimentally measured percolation thresholds from the literature (Beech et al., 2023). Filled black circles represent a single batch of previous experiments (Beech et al., 2023). Open white triangles and squares represent two new batches of experiments for the same gels. Error bars depict standard deviations. Horizontal dashed lines indicate the average across batches of intrinsic fracture energy for networks with only strong (black) or weak (red) strands.

linkers, against the percentage of strong linkers fed during gelation in Fig. 3b. For networks with uniformly strong (black) or weak (red) linkers, horizontal and vertical dashed lines denote fracture energies and percolation thresholds, respectively. Here, we report measured percolation thresholds for real networks from previously published experiments (Beech et al., 2023). Observe the nonlinear relationship between fracture energy and strong linker fraction. At low fractions, fracture energy plateaus despite the addition of strong linkers. Near the percolation threshold, the fracture energy increases towards that of a network with only strong linkers. At high fractions, the fracture energy of networks with some weak linkers can plateau near or potentially exceed that of a network without weak linkers.

4.2. Simulations

To further understand the fracture process of networks with hybrid bond strengths, we perform simulations to mimic the experimental measurements of fracture energy in hybrid networks with strong and weak linkers. In polymer-like network simulations, we randomly assign strands in 2D square lattices with strong and weak failure behavior. We restrict our attention to 2D systems to connect results to prior works on both percolated lattices and polymer network fracture. Note that different lattice topologies and dimensionalities give different percolation thresholds and fracture geometries (line cracks in 2D and planar cracks in 3D). Studies on 2D lattices indicate that the percolation threshold for a square lattice is $p_c = 0.5$ (Ziff, 1992), so for strong and weak strands, these concentrations match at $\phi_S = 50\%$. In contrast, the percolation threshold for 3D diamond lattices is $p_c = 0.388$ (Rubinstein et al., 2003). For simulations, directly assigning strand types alleviates any deviations or errors in concentrations from experiments caused by the gelation process. We individually characterize fracture energy and intrinsic fracture energy and display results across ratios of strong and weak strand types in Fig. 4. Values are normalized by the fracture energy of a network of only strong strands. In simulated networks with a single strand type, the fracture energy and intrinsic fracture energy are equivalent since strands are purely elastic and cracks propagate upon bridging strand rupture. Horizontal dashed lines denote the equal intrinsic fracture energies and fracture energies for lattices with only strong (black) or weak (red) strands. Vertical dashed lines denote the percolation thresholds. We observe a non-monotonic relationship between intrinsic fracture energy and fracture energy with respect to fraction of strong strands in polymer-like simulations. At low fractions and intermediate fractions of strong strands, both fracture energy metrics increase approximately linearly. Strikingly, with high fractions of strong strands, both surpass that of a pure network with only strong strands.

Beech et al. performed uniaxial stretching simulations of unnotched polymer networks with hybrid bond strengths that support experimental results (Beech et al., 2023); however, this measurement essentially revealed toughness, the absorbed energy per volume at the time of failure, instead of fracture energy, the resistance to crack growth. In addition, the previous simulations do not explain why the normalized fracture energy maintains a high level (≥ 1) at a high fraction of strong linkers ($\phi_{SL} \geq 75\%$). In their simulation, the trend of fracture energy has an S-shape, and no toughening effect was observed at high fractions of strong linkers. Multiple factors distinguish polymer and polymer-like network simulations. Unlike in the polymer-like network model, strands

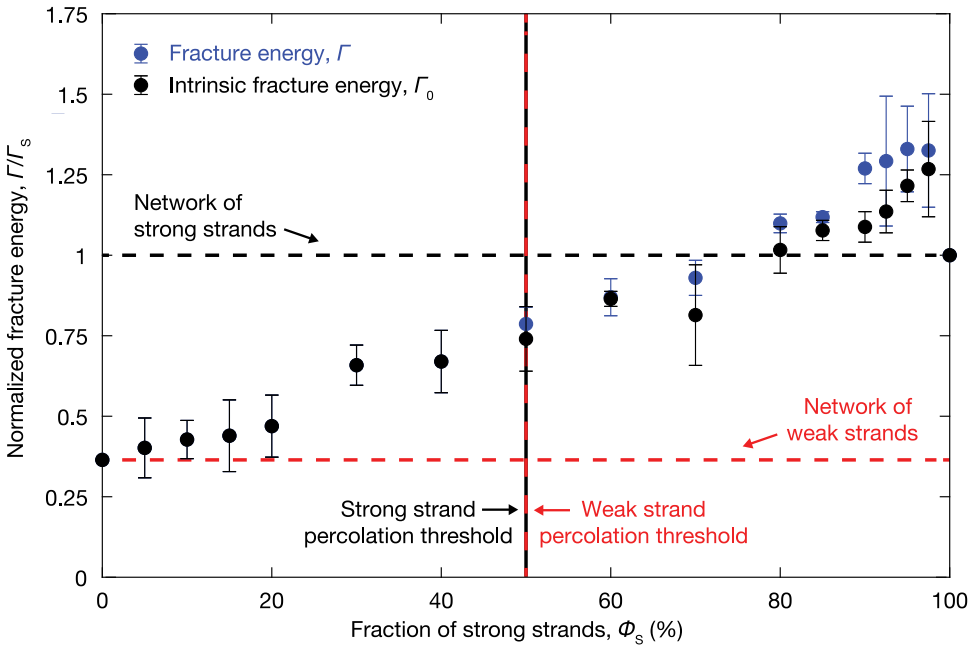

Fig. 4. Fracture energy (Γ, blue) and intrinsic fracture energy (Γ_0, black) measurements for simulated square polymer-like networks normalized by that of a network of strong strands (Γ_S) as a function of the fraction of strong strands in the network (ϕ_S). The vertical red and black dashed line marks the percolation threshold for both strong and weak strands.

can overlap in the coarse-grained simulation. Additionally, the coarse-grained simulation is in 3D with a more random network topology, while the numerical simulation here is in 2D with a lattice structure. As noted before, the measurements performed in each simulation type differ: coarse-grained polymer simulations measure a toughness of unnotched samples while polymer-like network simulations measure fracture energies from both notched and unnotched samples. However, experiments and simulations of polymer-like networks display that networks with some weak strands can outperform those with all strong strands. Polymer-like simulations and experiments also differ from polymer experiments. While we select tetra-PEG gels for experiments due to their model network architecture, low dispersity, and lack of trapped entanglements (Sakai et al., 2008; Beech et al., 2023), real polymers contain inhomogeneities like defects that differ from simulations. The 3D topologies of the gels also vary from the 2D square lattices of the polymer-like networks.

5. Discussion

5.1. Crack growth phenomena

To elucidate the connection between concentrations of strand types, connectivity, and fracture energies, we visualize the crack growth behaviors within the zone surrounding the tip of the precut crack to explore the underlying physics behind contributions to intrinsic fracture energy across strong strand fractions in polymer-like network simulations. The image in Fig. 5a depicts the network connectivity (2D square lattice) with delineated strand types (strong = black, weak = red) of a 75 × 105 layer region around a notch within a representative sample in the undeformed configuration. When deformed to some height h, strands near the crack tip stretch as depicted in Fig. 5b. As the crack propagates, we map locations of broken strands onto the undeformed lattice as shown in Fig. 5c for clarity in depicting crack growth. The deformed configuration during crack propagation (Fig. 5d) can also be plotted.

We provide maps of the fracture paths in the undeformed configuration in four ranges: low ϕ_S (I, 10% and 20%), intermediate ϕ_S below percolation (II, 30% and 40%), intermediate ϕ_S above percolation (III, 60% and 70%), and high ϕ_S (IV, 80% and 90%). We select a representative sample for both concentrations within the regime. For each case, we illustrate the crack progression at four loading steps during a pure shear fracture test. Samples are loaded vertically with a horizontal edge crack spanning half of the sample width ($w_0/2$). The first step displays the notched specimen in the undeformed configuration at h_0. The second maps an intermediate sample height where at least one strand has ruptured but $h < h_c$. The third marks all broken strands at h_c. The fourth depicts a sample height past h_c where the crack has propagated further into the bulk material. All crack path maps in Figs. 5–9 display a 75 × 105 layer subregion near the crack tip of the 150 × 300 layer samples.

In regime I, visualizations depict that cracks predominantly propagate by traversing through layers of weak strands. Images in Fig. 6a and Fig. 6b show representative samples at ϕ_S = 10% and 20%, which display similar trends. The cracks first initiate

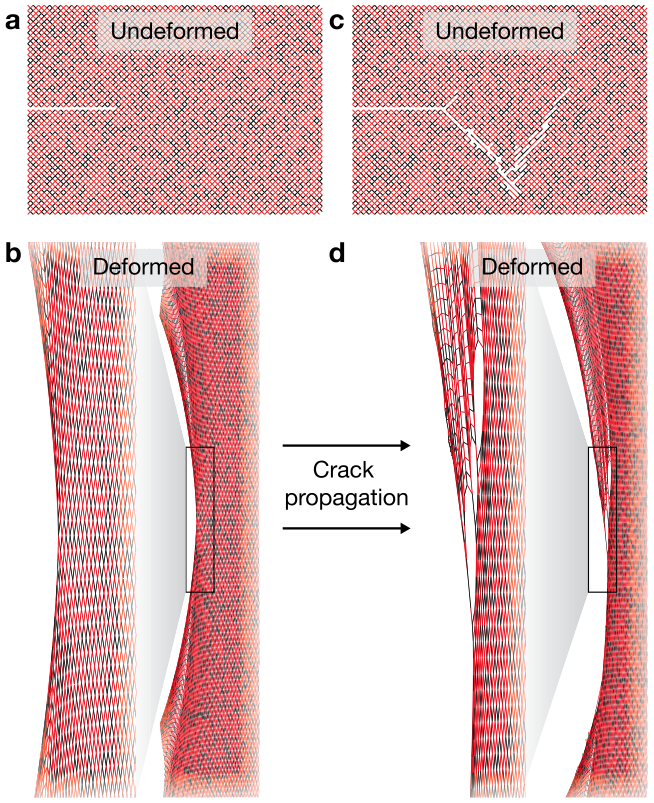

Fig. 5. (a) Hybrid networks are depicted in the undeformed configuration for visualization to represent the (b) deformed configuration. As a crack propagates, the (c) undeformed configuration maps the crack path from the corresponding (d) deformed sample. Representative images display results from simulations at $\phi_S = 30\%$.

before h_c. They then travel approximately along a single line through layers of weak strands. Finally, past h_c, they continue to advance through the material and primarily break weak strands. Cracks propagate along layers at approximately 45 degree angles in the undeformed mapping due to lattice geometry. Note that with increasing strong strand fractions, the crack maintains a relatively linear path but shifts between layers to avoid fracturing strong strands. Samples with no strong strands also fracture by predominantly severing a single weak layer. The addition of some strong strands does not strongly influence this fracture path. Fracture energies of these samples increase nearly linearly with strong strand concentration.

In regime II, results show cracks deflecting or splitting upon impedance by clusters of strong strands. The crack tip regions for samples at $\phi_S = 30\%$ and 40% are shown in Fig. 7a and Fig. 7b, respectively. The cracks initiate along a single layer like in regime I before h_c but can be redirected as they grow if they encounter strong cluster blockades. One case in Fig. 7a at $\phi_S = 30\%$ approximately displays a 90 degree deflection in the mapping, instigating propagation along a layer of strands perpendicular to the initiated crack. A second case in Fig. 7b at $\phi_S = 40\%$ shows branched fracture as a single crack splits into two separate perpendicular cracks. One of the remaining cracks deflects again further along. The fracture energy ascends approximately linearly within this regime.

In regime III, we observe cracks pinning — where obstacles suppress their growth — when they reach a large strong cluster. Mappings in Fig. 8a and Fig. 8b exhibit the crack growth of networks with $\phi_S = 60\%$ and 70%, respectively. The cracks initially either remain stagnant or grow slightly by breaking a few strands. At this point, the cracks remain pinned while a few weak strands sacrificially break away from the crack path. Past h_0, the cracks overcome the fully connected strong barrier and propagate into the material. Cracks in regimes II and III can exhibit branched fracture, as characterized by cracks that split and branch along multiple planes. Recall from Fig. 4 that the fracture energy continues to linearly increase past the percolation threshold and nears the fracture energy of a homogeneous strong network.

In regime IV, mappings display cracks blunting before advancing into the material. Instead of advancing the crack, the loaded networks first forfeit an excess of weak strands outside of the line crack. This creates a damage zone around the crack tip. The densely percolated strong networks preclude cracks enough to enable deformations past the point where weak strand rupture can occur. Eventually, past h_c, cracks overcome this barrier and propagate through the damage zone of disproportionately strong strands. Fig. 4 indicates that a fracture energy overshoot occurs at these values of ϕ_S; networks with some weak strands exhibit increased fracture energy with respect to those without any weak strands. We suspect this overshoot occurs due to the crack blunting behavior. Stress

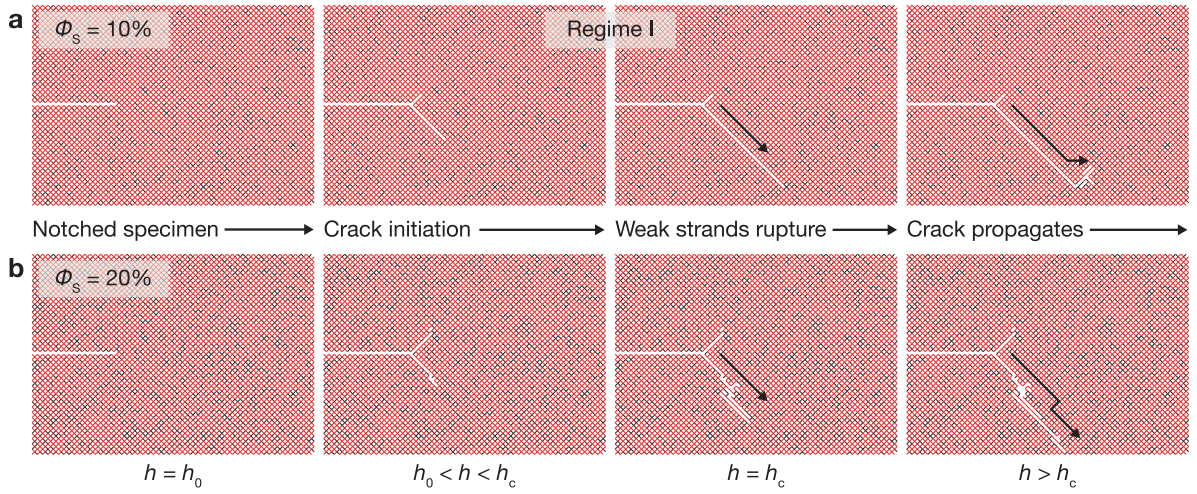

Fig. 6. Regime I. The crack propagates with minimal resistance through layers of weak strands in networks with low fractions of strong strands. Images depict fracture paths through samples with (a) $\phi_S = 10\%$ and (b) $\phi_S = 20\%$ during notched loading from the undeformed sample height (h_0) through the critical height (h_c). Strong (black) and weak (red) strands are visualized in the undeformed configuration.

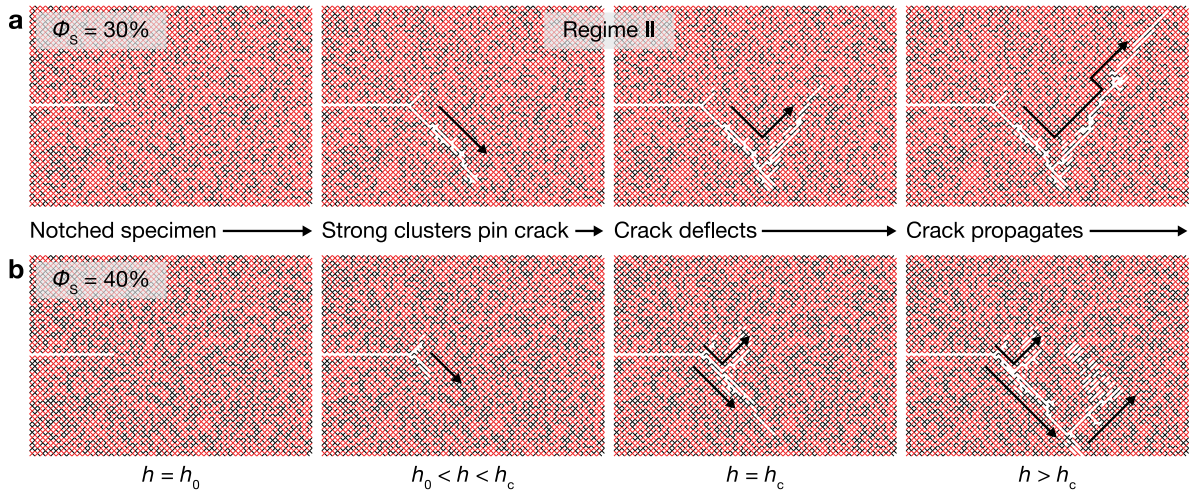

Fig. 7. Regime II. The crack deflects when it reaches some structure of connected strong strands in networks. Images depict fracture paths through samples with (a) $\phi_S = 30\%$ and (b) $\phi_S = 40\%$ during notched loading from the undeformed sample height (h_0) through the critical height (h_c). Strong (black) and weak (red) strands are visualized in the undeformed configuration.

redistribution can strengthen (Mulla et al., 2022) and improve fatigue resistance (Steck et al., 2023) in polymer networks. Here, weak strand sacrifice can deconcentrate stress buildup in the bridging strands at the tips of a cracks. Recent molecular dynamics simulations show similar behaviors in polymer networks with carefully placed dangling chains (Wang et al., 2024b). This enables networks to achieve enhanced extensibility before failure by crack growth. It is also noteworthy that weak strand sacrifice increases the average loop size during crack propagation, which gives a heightened fracture energy in theoretical models (Lake and Thomas, 1967; Deng et al., 2023; Hartquist et al., 2024; Wang et al., 2024a).

5.2. Fracture energy overshoot

We store the location and type of each strand that breaks during fracture of hybrid networks in simulations. We plot the total number (n_x) — distinguished by strand type — of strands that break with respect to strong strand fraction before the sample reaches h_c in Fig. 10. First, results indicate that weak strand failure dominates throughout the fracture process. This aligns with growth patterns in Figs. 6–9, where crack paths prefer to traverse through or forfeit weak strands before bulk failure. Second, the number of broken strands in networks with a few weak strands far exceeds that of networks with many weak strands. This metric highlights the extent of strand sacrifice near the peak fracture energy measurements. Results corroborate the premise that weak strand sacrifice can redistribute stress around a crack, further justifying the fracture energy overshoot.

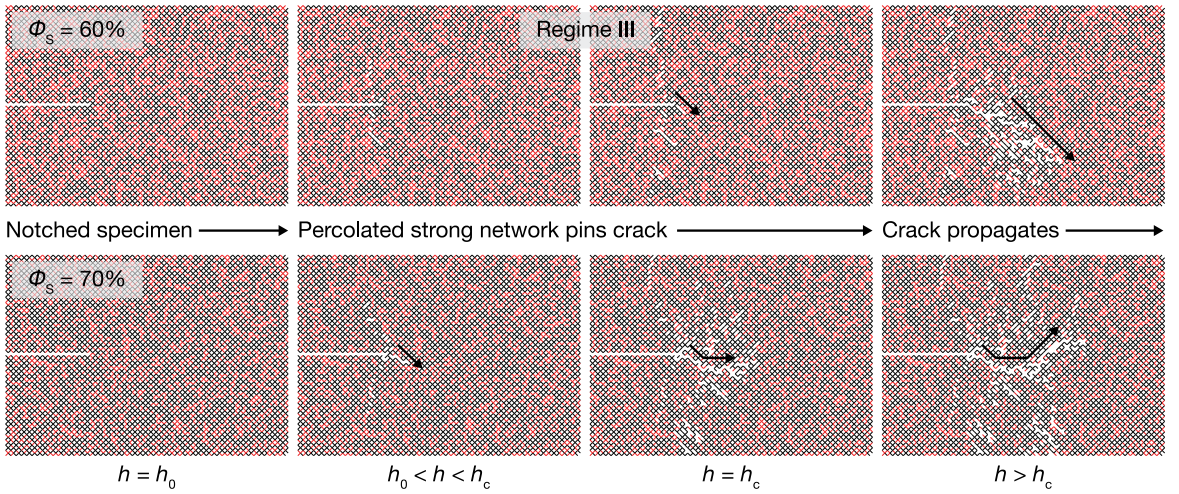

Fig. 8. Regime III. The crack pins in samples with strong strand fractions greater than the percolation threshold, which causes local weak strand sacrifice and suggests that percolated structures may further restrict crack growth. Images depict fracture paths through samples with (a) $\phi_S = 60\%$ and (b) $\phi_S = 70\%$ during notched loading from the undeformed sample height (h_0) through the critical height (h_c). Strong (black) and weak (red) strands are visualized in the undeformed configuration.

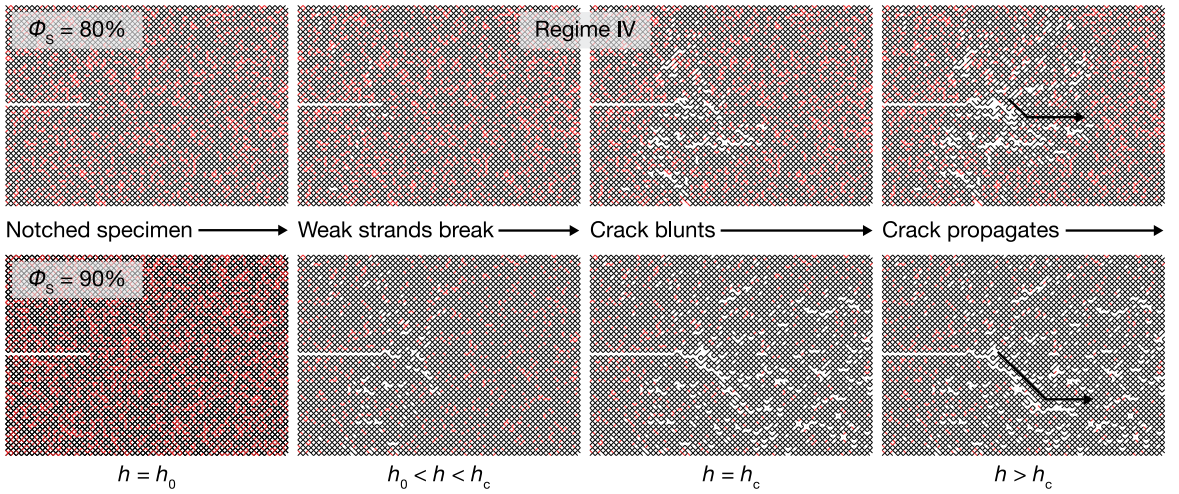

Fig. 9. Regime IV. The crack blunts in networks with very low fractions of weak strands, which causes substantial and efficient weak strand sacrifice within a damage zone. Images depict fracture paths through samples with (a) $\phi_S = 80\%$ and (b) $\phi_S = 90\%$ during notched loading from the undeformed sample height (h_0) through the critical height (h_c). Strong (black) and weak (red) strands are visualized in the undeformed configuration.

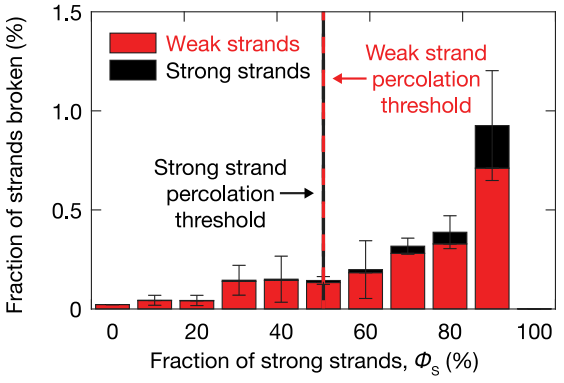

Fig. 10. The fraction of strong (black) and weak (red) strands broken in a notched specimen before the sample reaches its critical height (h_c) at different strong strand fractions (ϕ_S).

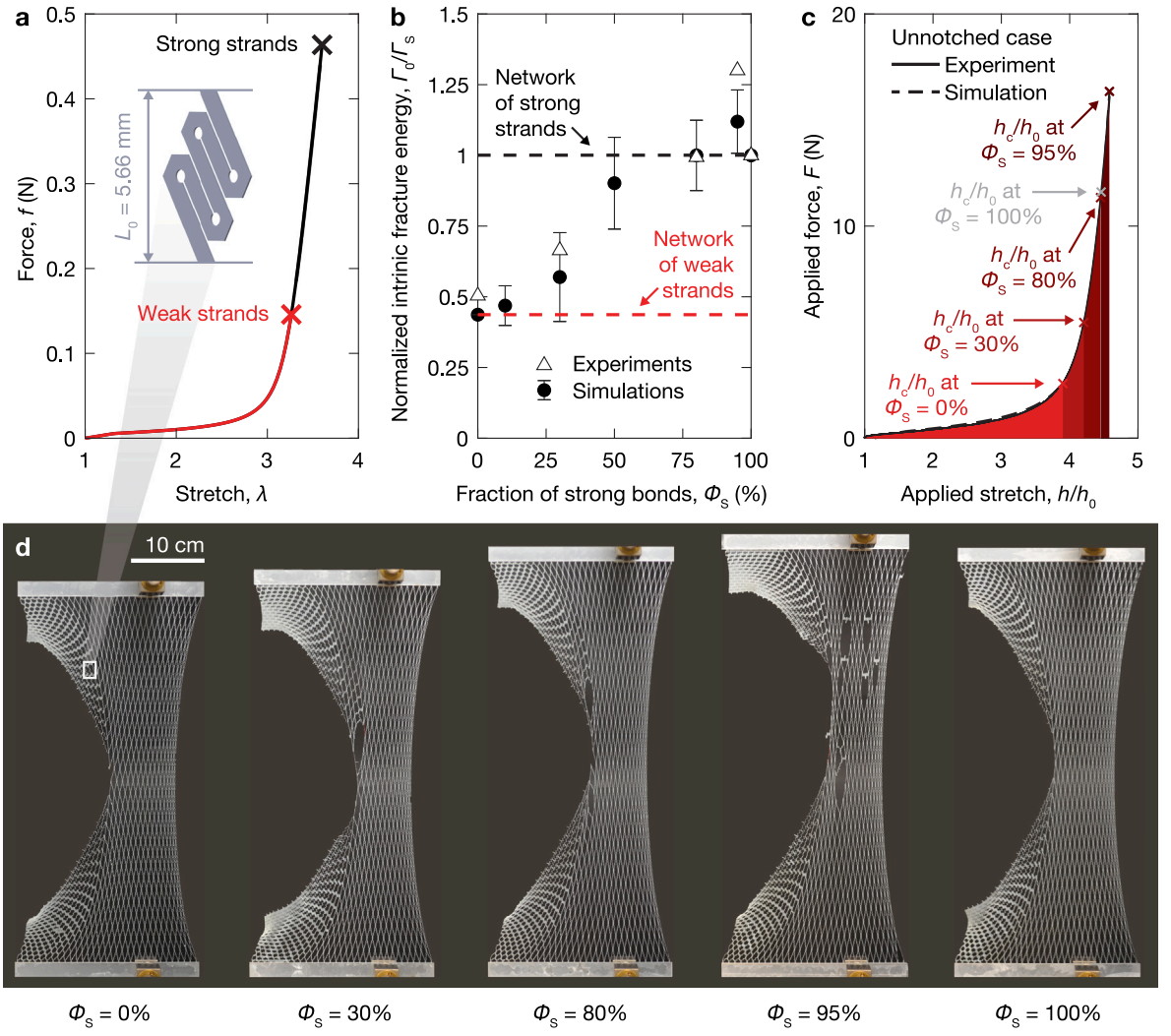

Fig. 11. Experimental validation of the fracture energy trends for polymer-like networks with hybrid bond strengths in 2D architected square lattices. (a) The force-stretch response of individual strong and weak strands within the architected networks, which unfold before stretching to attain a J-shaped curve. (b) Intrinsic fracture energy (Γ_0) measurements for experimental (open triangles) and simulated (filled circles) networks normalized by that of a network of strong strands (Γ_S) as a function of the fraction of strong strands in the network (ϕ_S). Error bars give variations across random distributions of strong and weak strands. (c) Results are measured via the approximate pure shear test by loading notched and unnotched samples to the critical height h_c for experiments (solid line) and simulations (dashed line). (d) Notched experimental samples with ϕ_S = 0%, 30%, 80%, 95%, and 100% loaded to the critical height h_c.

We further perform experiments on macroscopic architected materials to validate fracture energy trends, including the overshoot. Polymer-like strand behavior can be achieved by designing ribbon or zigzag shaped patterns from thin films. The pattern enables a soft initial response during unfolding while the material provides a stiffer terminal response during stretching (Jang et al., 2015; Deng et al., 2023). This provides J-shaped force stretch behavior which mimics polymer chains. We fabricate strands with strong and weak bond strengths such that the ratio of fracture forces $f_f^S/f_f^W = 2.5$ (Fig. 11a). Recall that $f_f^S/f_f^W \approx 4$–6 in polymer experiments and $f_f^S/f_f^W = 5$ in polymer-like simulations. We then assemble those strands into 2D square lattices and produce networks by laser cutting patterns onto acetal films. Tensile tests on unnotched samples give the material force-stretch loading response. Tests on notched samples give the critical height h_c for crack propagation. Samples are designed such that h_c at ϕ_S = 95% and ϕ_S = 100% do not exceed the height where the first strand breaks in an unnotched network at ϕ_S = 0%. This condition guarantees that the measurement from the approximate pure shear test gives the intrinsic fracture energy regardless of weak strand placement within a hybrid network. We test five network types at ϕ_S = 0%, 30%, 80%, 95%, and 100%. We measure intrinsic fracture energy using the approximate pure shear test and compare results to simulations in Fig. 11b. Results notably indicate that the critical stretch of a notched sample with 5% weak strands reaches 4.58, surpassing the critical stretch for a sample with only strong strands of 4.47, as shown in Fig. 11c. The measured intrinsic fracture energy of the hybrid network exceeds that of a pure network of strong strands, yielding $\Gamma_0(\phi_S = 95\%)/\Gamma_0(\phi_S = 100\%) = 1.28$. Images display representative notched samples at h_c in Fig. 11d.

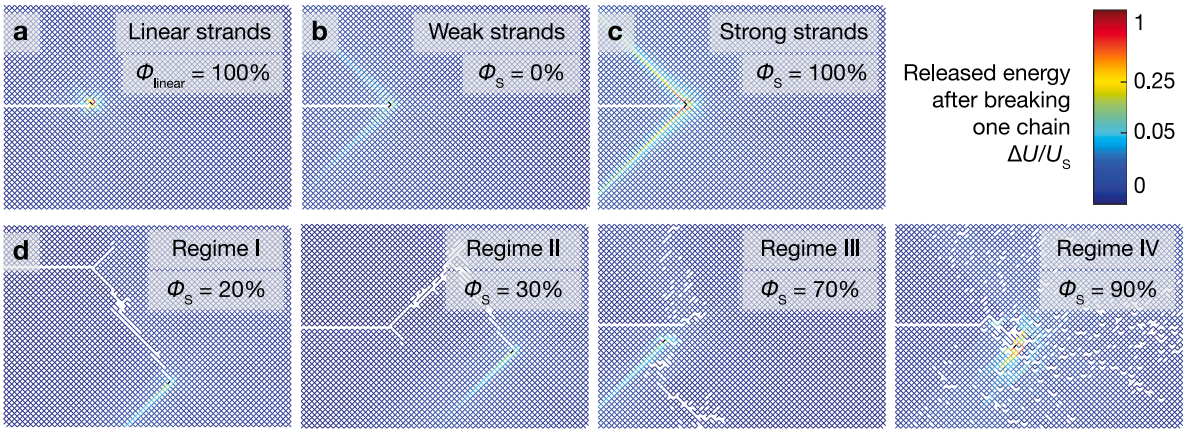

Fig. 12. Energy released by each strand after a strand breaks. Networks of strands with (a) linear force-stretch relationships (fraction of linear strands ϕ_{linear} = 100%) compared with those of (b) weak, (c) strong strands, and (d) varying fractions of strong strands (ϕ_S = 20%, 30%, 70%, and 90%), representing regimes I-IV. Note that the released energy ΔU for networks of linear strands are normalized by U_{linear}, while all others are normalized by U_S.

5.3. Nonlocal energy release

To further elucidate the details of hybrid polymer-like network fracture, we capture the strain energy distributions near the crack tip throughout the fracture process. We characterize the change in stored energy right before and after one strand ruptures at h_c — termed the released energy (20) — to examine the degree of chain relaxation that occurs around the crack. The released energy is normalized by the work to rupture one strong strand, which is computed as the stored energy (19) at λ_f. We map this quantity onto the undeformed configuration in Fig. 12 for strands surrounding the crack tip.

Alongside polymer-like hybrid networks, we study a control sample comprised of strands with linear elasticity yet the same f_f and λ_f as strong strands in Fig. 12a. Note that for the linear control, we normalize released energy by the work to rupture a linear strand (instead of U_S). For such networks, the majority of released energy is contained within a few strands surrounding the crack. This matches the physical pictures provided by Griffith and Lake-Thomas that the stress concentrations restrict fracture to single layers. In contrast, homogeneous networks of weak (Fig. 12b) and strong polymer-like strands (Fig. 12c) display bands of nonlocal energy release extending into the network continuum. These energy release bands extend at angles due to the geometry of the loading on the deformed crack tip. Since $U_W < U_S$, these polymer-like cases display differences in energy release magnitude but give similar qualitative trends. These results match the nonlocal energy release model (Deng et al., 2023).

Applied to networks with hybrid bond strengths, Fig. 12d shows released energy in samples across strong strand fractions (ϕ_S = 20%, 30%, 70%, and 90%). Note that for the pure networks with linear, weak, and strong strands, the bridging strand that breaks at h_c resides at the tip of the precut crack. In contrast, hybrid networks break more strands before the critical stretch (see Fig. 10a), displacing the crack tip at h_c. Nonetheless, in hybrid networks, some strands far from the crack tip release large portions of stored energy. Models suggest that these nonlocal contributions can cause orders of magnitude enhancements in measured fracture energies compared to cases where only strands near the crack tip release substantial energy (Deng et al., 2023; Hartquist et al., 2024; Wang et al., 2024a). Therefore, the nonlocal result matches quantitative findings, for the fracture energies of hybrid and uniform networks reside on the same order of magnitude.

6. Concluding remarks

We systematically study the fracture mechanics of hybrid polymer-like networks with varying ratios of two strand types containing different rupture forces. Experiments realize polymer networks with hybrid bond strengths by tuning the feeding ratio of two mechanophores with distinct reactivities used to crosslink tetra-PEG gels and result in a nonlinear relationship between fracture energy and linker type ratios. These findings motivate polymer-like experiments and simulations which impose two types of PEG-like force-stretch behaviors — parametrized by the m-FJC model — with different rupture forces on edges of polymer-like 2D square lattices. Network-level experiments and simulations indicate that the fracture energies can also follow nonlinear trends with respect to strand type ratios. Notably, polymer-like networks with some weak strands can attain higher intrinsic fracture energy than those entirely comprised of strong strands. Macroscopic experiments on architected materials implement two types of folded strands into square patterns and validate the fracture energy enhancement.

To better connect fracture energy measurements of polymer-like networks with the concentrations of each strand type, we investigate the strand-level details driving bulk mechanical failure by crack propagation. Simulations illustrate the failure process by supplying the locations, order, type, and quantity of strands that break to advance an edge crack. We observe four varieties of fracture behaviors depending on the concentrations of each strand type. In networks with relatively few strong strands, cracks traverse along layers of weak strands, deviating only slightly to avoid sparse strong strands. With increasing strong strand fraction,

cracks begin to deflect, and the fracture energy rises. As clusters of strong strands grow, sufficiently large structures of strong strands can pin crack growth and enable a few weak strands to break near the crack tip. The quantitative correlations between cluster size and fracture behaviors remain underexplored. Once the fraction of weak strands becomes small enough, the fracture energy notably eclipses that of a pure strong network. Weak strands fail throughout a damage zone around the bridging strand, which blunts the crack. Weak strand sacrifice could cause this fracture energy enhancement by increasing average loop size and deconcentrating stress at the tip. This transition notably aligns with the approximate concentration where aggregate weak clusters are separated into isolated strands, which could give rise to more efficient sacrifice and loop opening. In all cases for both uniform and hybrid polymer-like networks, strain energy distributions indicate that strands far from the crack tip contribute nonlocal energy release during failure.

These findings offer a foundation for understanding the impact of bond strength on fracture mechanisms in polymer-like networks. They also provide mechanistic strategies for fabricating materials with tailored properties. Tuning the $f_{\mathrm{f}}^{\mathrm{S}}/f_{\mathrm{f}}^{\mathrm{W}}$ ratio, force-stretch strand responses, strand type concentrations, and network topology provides a framework to further optimize the fracture energy overshoot for accentuating crack suppression mechanisms and revealing extreme mechanical performance. Future works could additionally provide models to parameterize key features of the fracture energy overshoot and link clustering behaviors or probabilities with crack paths. Overall, this battery of experiments and simulations provides insights into the connection between the molecular details and bulk fracture behaviors of soft materials. Conclusions from polymer-like network studies can directly give intuitions into soft architected network fracture and indirectly shed light on trends related to polymer failure. Real polymeric materials contain additional complexities like molecular interactions, defects, and polydispersity, which could possibly explain variations in specific results, such as the concentrations with peak performance. Nonetheless, polymer-like networks can efficiently capture energetic effects due to large deformations, which can dominate during crack propagation in polymers. As techniques to modulate chain connectivity (Sakai et al., 2008; Zhukhovitskiy et al., 2016), conformation (Hartquist et al., preprint), entanglement (Kim et al., 2021), and reactivity (Wang et al., 2023) in polymer networks advance, studies like these harnessing polymer-like analogs offer a platform to further elucidate the fundamental mechanisms driving enhanced performance. In addition, this work can facilitate the design of tough polymer, polymer-like, and metamaterial networks with mechanisms that intrinsically resist failure, spanning applications from biomaterials to spacecraft.

CRediT authorship contribution statement

Chase M. Hartquist: Writing – review & editing, Writing – original draft, Visualization, Validation, Software, Methodology, Investigation, Formal analysis, Data curation, Conceptualization. **Shu Wang:** Writing – review & editing, Methodology, Investigation, Formal analysis, Conceptualization. **Bolei Deng:** Writing – review & editing, Validation, Software, Methodology. **Haley K. Beech:** Methodology, Investigation, Formal analysis. **Stephen L. Craig:** Writing – review & editing, Validation, Supervision, Project administration. **Bradley D. Olsen:** Writing – review & editing, Validation, Supervision, Project administration. **Michael Rubinstein:** Writing – review & editing, Visualization, Validation, Supervision, Project administration, Methodology. **Xuanhe Zhao:** Writing – review & editing, Investigation, Funding acquisition, Formal analysis.

Declaration of competing interest

The authors declare the following financial interests/personal relationships which may be considered as potential competing interests: The authors declare that they have no competing financial interests or personal relationships that could have appeared to influence the work reported in this paper.

Acknowledgments

The authors acknowledge the MIT SuperCloud and Lincoln Laboratory Supercomputing Center for providing HPC resources that have contributed to the research results reported within this paper. This work was supported in part by the National Institutes of Health (1R01HL153857-01 and 1R01HL167947-01 to X.Z. and P01-HL164320 to M.R.), Department of Defense Congressionally Directed Medical Research Programs (PR200524P1 to X.Z.), the National Science Foundation (EFMA-1935291 to X.Z.), and the NSF Center for the Chemistry of Molecularly Optimized Networks (MONET) (CHE-2116298 to S.L.C, B.D.O., M.R.). C.M.H. acknowledges support from the NSF Graduate Research Fellowship and the MathWorks Fellowship.

Appendix

A.1. Visualizing networks with hybrid bond strengths

We systematically vary the ratio of strand types in simulations through random assignment. Fig. A.13 displays portions of representative samples at $\phi_{\mathrm{S}} = 0\%$, 20%, 40%, 60%, 80%, and 100%. Weak (red) and strong (black) strand types with constitutive behaviors defined in Fig. 1 comprise 2D square lattices.

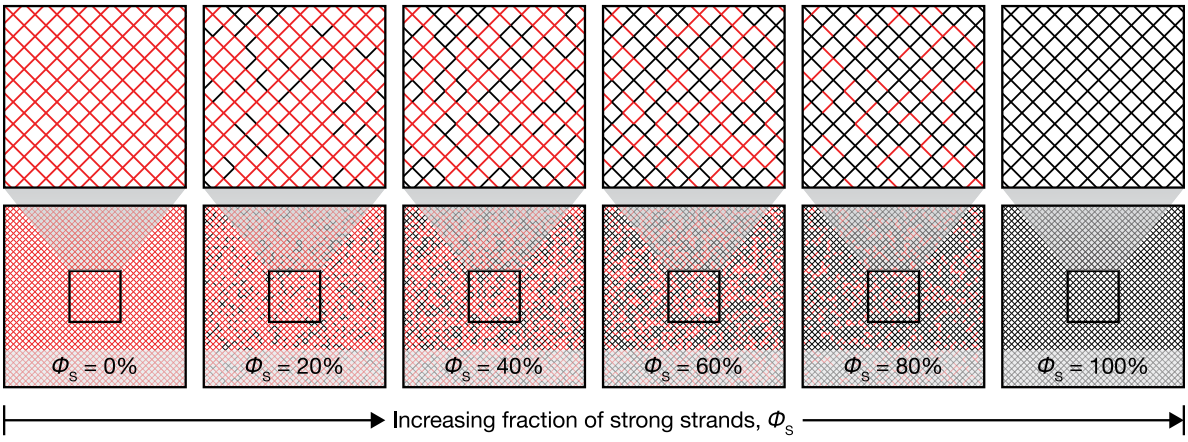

Fig. A.13. Representative images of hybrid polymer-like networks with fractions of strong strands ϕ_S ranging from 0% to 100%.

A.2. Scaling of intrinsic fracture energy with strand fracture force

We report simulation results for samples with $h = 150 \times w = 300$ layers of repeating strands to provide sufficient size to observe complex fracture processes while preserving computational efficiency. Our group previously noted that polymer-like networks with PEG-like strand behavior can require up to 10^3 repeating layers to achieve fully converged intrinsic fracture energy calculations (Deng et al., 2023). These results highlighted prospective justifications for the difference in measured intrinsic fracture energy of polymer networks compared to the Lake-Thomas model from (2). Extensive simulations and experiments validated an alternative scaling for intrinsic fracture energy as

$$\Gamma_0/M \propto f_f L_f, \tag{A.1}$$

where L_f is the length of strands at rupture (Hartquist et al., 2024). To further assess this model and validate our current simulation results, we perform additional simulations on networks with 500 × 1000 repeating layers of homogeneous strands with f_f = 1 nN, 2 nN, 3 nN, 4 nN, and 5 nN (Fig. A.14). The pure shear test provides the intrinsic fracture energy of these networks. The intrinsic fracture energy, normalized by that of a network of strong strands with f_f = 5 nN, is plotted against f_f compared with the proportionality provided by the nonlocal model in (A.1).

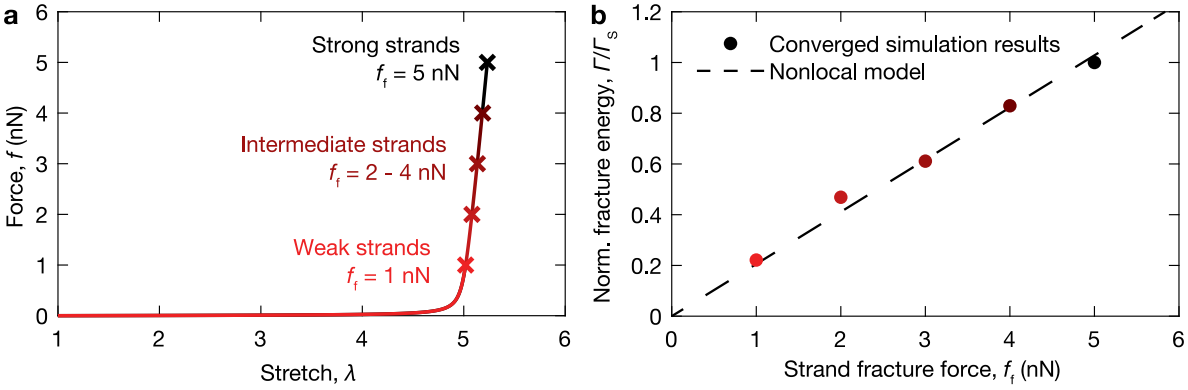

Fig. A.14. Square lattices containing strictly (a) weak, intermediate, or strong strands with fracture forces f_f = 1 nN, 2 nN, 3 nN, 4 nN, and 5 nN achieve (b) intrinsic fracture energies Γ_0 which scale linearly with the strand fracture force f_f in simulations of polymer-like networks with 500 × 1000 repeating layers of homogeneous strands.

Data availability

Data will be made available on request.

References

Akagi, Y., Gong, J.P., Chung, U.i., Sakai, T., 2013. Transition between phantom and affine network model observed in polymer gels with controlled network structure. Macromolecules 46 (3), 1035–1040.

Arora, A., Lin, T.S., Beech, H.K., Mochigase, H., Wang, R., Olsen, B.D., 2020. Fracture of polymer networks containing topological defects. Macromolecules 53 (17), 7346–7355.

Bai, R., Yang, J., Suo, Z., 2019. Fatigue of hydrogels. Eur. J. Mech. A Solids 74, 337–370.

Barney, C.W., Ye, Z., Sacligil, I., McLeod, K.R., Zhang, H., Tew, G.N., Riggleman, R.A., Crosby, A.J., 2022. Fracture of model end-linked networks. Proc. Natl. Acad. Sci. 119 (7), e2112389119.

Beech, H.K., Wang, S., Sen, D., Rota, D., Kouznetsova, T.B., Arora, A., Rubinstein, M., Craig, S.L., Olsen, B.D., 2023. Reactivity-guided depercolation processes determine fracture behavior in end-linked polymer networks. ACS Macro Lett. 12 (12), 1685–1691.

Borodulina, S., Motamedian, H.R., Kulachenko, A., 2018. Effect of fiber and bond strength variations on the tensile stiffness and strength of fiber networks. Int. J. Solids Struct. 154, 19–32.

Bowser, B.H., Wang, S., Kouznetsova, T.B., Beech, H.K., Olsen, B.D., Rubinstein, M., Craig, S.L., 2021. Single-event spectroscopy and unravelling kinetics of covalent domains based on cyclobutane mechanophores. J. Am. Chem. Soc. 143 (13), 5269–5276.

Creton, C., Ciccotti, M., 2016. Fracture and adhesion of soft materials: a review. Rep. Progr. Phys. 79 (4), 046601.

Deng, B., Wang, S., Hartquist, C., Zhao, X., 2023. Nonlocal intrinsic fracture energy of polymerlike networks. Phys. Rev. Lett. 131 (22), 228102.

Deogekar, S., Picu, R., 2018. On the strength of random fiber networks. J. Mech. Phys. Solids 116, 1–16.

Flory, P.J., 1942. Constitution of three-dimensional polymers and the theory of gelation.. J. Phys. Chem. 46 (1), 132–140.

Ghareeb, A., Elbanna, A., 2020. An adaptive quasicontinuum approach for modeling fracture in networked materials: Application to modeling of polymer networks. J. Mech. Phys. Solids 137, 103819.

Griffith, A.A., 1921. VI. The phenomena of rupture and flow in solids. Philos. Trans. R. Soc. London Ser. A 221 (582–593), 163–198.

Hartquist, C.M., Lin, S., Zhang, J.H., Wang, S., Rubinstein, X., 2023. An elastomer with ultrahigh strain-induced crystallization. Sci. Adv. 9 (50), eadj0411.

Hartquist, C., Wang, S., Cui, Q., Matusik, W., Deng, B., Zhao, X., 2024. A universal scaling law for intrinsic fracture energy of networks. arXiv preprint arXiv:2401.05564.

Jang, K.I., Chung, H.U., Xu, S., Lee, C.H., Luan, H., Jeong, J., Cheng, H., Kim, G.T., Han, S.Y., Lee, J.W., et al., 2015. Soft network composite materials with deterministic and bio-inspired designs. Nature Commun. 6 (1), 6566.

Kim, J., Zhang, G., Shi, M., Suo, Z., 2021. Fracture, fatigue, and friction of polymers in which entanglements greatly outnumber cross-links. Science 374 (6564), 212–216.

Lake, G., Thomas, A., 1967. The strength of highly elastic materials. Proc. R. Soc. London Ser. A 300 (1460), 108–119.

Lei, J., Li, Z., Xu, S., Liu, Z., 2021. A mesoscopic network mechanics method to reproduce the large deformation and fracture process of cross-linked elastomers. J. Mech. Phys. Solids 156, 104599.

Lei, J., Liu, Z., 2022. A network mechanics method to study the mechanism of the large-deformation fracture of elastomers. J. Appl. Phys. 132 (13).

Lin, S., Zhao, X., 2020. Fracture of polymer networks with diverse topological defects. Phys. Rev. E 102 (5), 052503.

Malakhovsky, I., Michels, M., 2007. Effect of disorder strength on the fracture pattern in heterogeneous networks. Phys. Rev. B—Condens. Matter Mater. Phys. 76 (14), 144201.

Mao, Y., Talamini, B., Anand, L., 2017. Rupture of polymers by chain scission. Extreme Mech. Lett. 13, 17–24.

Mulla, Y., Avellaneda, M.J., Roland, A., Baldauf, L., Jung, W., Kim, T., Tans, S.J., Koenderink, G.H., 2022. Weak catch bonds make strong networks. Nature Mater. 21 (9), 1019–1023.

Oesterhelt, F., Rief, M., Gaub, H., 1999. Single molecule force spectroscopy by AFM indicates helical structure of poly (ethylene-glycol) in water. New J. Phys. 1 (1), 6.

Picu, R., Jin, S., 2023. Toughness of network materials: Structural parameters controlling damage accumulation. J. Mech. Phys. Solids 172, 105176.

Rivlin, R., Thomas, A.G., 1953. Rupture of rubber. I. Characteristic energy for tearing. J. Polym. Sci. 10 (3), 291–318.

Rubinstein, M., Colby, R.H., et al., 2003. Polymer Physics, Vol. 23, Oxford University Press New York.

Sakai, T., Matsunaga, T., Yamamoto, Y., Ito, C., Yoshida, R., Suzuki, S., Sasaki, N., Shibayama, M., Chung, U.i., 2008. Design and fabrication of a high-strength hydrogel with ideally homogeneous network structure from tetrahedron-like macromonomers. Macromolecules 41 (14), 5379–5384.

Smith, S.B., Cui, Y., Bustamante, C., 1996. Overstretching B-DNA: the elastic response of individual double-stranded and single-stranded DNA molecules. Science 271 (5250), 795–799.

Stauffer, D., Aharony, A., 2018. Introduction to Percolation Theory. Taylor & Francis.

Steck, J., Kim, J., Kutsovsky, Y., Suo, Z., 2023. Multiscale stress deconcentration amplifies fatigue resistance of rubber. Nature 624 (7991), 303–308.

Stockmayer, W.H., 1943. Theory of molecular size distribution and gel formation in branched-chain polymers. J. Chem. Phys. 11 (2), 45–55.

Talamini, B., Mao, Y., Anand, L., 2018. Progressive damage and rupture in polymers. J. Mech. Phys. Solids 111, 434–457.

Tang, J., Li, J., Vlassak, J.J., Suo, Z., 2017. Fatigue fracture of hydrogels. Extreme Mech. Lett. 10, 24–31.

Wang, S., Beech, H.K., Bowser, B.H., Kouznetsova, T.B., Olsen, B.D., Rubinstein, M., Craig, S.L., 2021. Mechanism dictates mechanics: a molecular substituent effect in the macroscopic fracture of a covalent polymer network. J. Am. Chem. Soc. 143 (10), 3714–3718.

Wang, S., Hartquist, C.M., Deng, B., Zhao, X., 2024a. A loop-opening model for the intrinsic fracture energy of polymer networks. Macromolecules.

Wang, S., Hu, Y., Kouznetsova, T.B., Sapir, L., Chen, D., Herzog-Arbeitman, A., Johnson, J.A., Rubinstein, M., Craig, S.L., 2023. Facile mechanochemical cycloreversion of polymer cross-linkers enhances tear resistance. Science 380 (6651), 1248–1252.

Wang, S., Panyukov, S., Rubinstein, M., Craig, S.L., 2019. Quantitative adjustment to the molecular energy parameter in the lake–Thomas theory of polymer fracture energy. Macromolecules 52 (7), 2772–2777.

Wang, X., Zhao, S., Xu, X., 2024b. Molecular dynamics study on the stress concentration in polymer networks with dangling chains. J. Phys. Chem. B.

Yamaguchi, T., Onoue, Y., Sawae, Y., 2020. Topology and toughening of sparse elastic networks. Phys. Rev. Lett. 124 (6), 068002.

Zhang, W., Zhang, X., 2003. Single molecule mechanochemistry of macromolecules. Prog. Polym. Sci. 28 (8), 1271–1295.

Zhao, X., 2014. Multi-scale multi-mechanism design of tough hydrogels: building dissipation into stretchy networks. Soft Matter 10 (5), 672–687.

Zhao, X., Chen, X., Yuk, H., Lin, S., Liu, X., Parada, G., 2021. Soft materials by design: unconventional polymer networks give extreme properties. Chem. Rev. 121 (8), 4309–4372.

Zhukhovitskiy, A.V., Zhong, M., Keeler, E.G., Michaelis, V.K., Sun, J.E., Hore, M.J., Pochan, D.J., Griffin, R.G., Willard, A.P., Johnson, J.A., 2016. Highly branched and loop-rich gels via formation of metal–organic cages linked by polymers. Nature Chem. 8 (1), 33–41.

Ziff, R.M., 1992. Spanning probability in 2D percolation. Phys. Rev. Lett. 69 (18), 2670.